Mechanics of Materials 195 (2024) 105031

Contents lists available at ScienceDirect

Mechanics of Materials

journal homepage: www.elsevier.com/locate/mecmat

Research paper

A mathematical model to design pillar-shaped bioinspired mechanical sensors

A. Solis [a], L. Alonso [b,*]

[a] Department of Mechanical Engineering and Industrial Design, University of Cádiz, Avda. de la Universidad de Cádiz 10, 11519, Puerto Real (Cádiz), Spain
[b] Durability and Mechanical Integrity of Structural Materials, Rey Juan Carlos University, C/Tulipán s.n., 28933, Spain

ARTICLE INFO

Keywords:
Soft materials
Wire dynamics
Mechanical sensors
Bioinspired materials
Mechanical behaviour

ABSTRACT

Soft robots and sensor/actuator systems are often based on bioinspired designs to leverage nature patterns. Specifically, pillar-shaped sensors are useful for human activity monitoring, locomotion of soft robots or treatment of cardiovascular diseases. If electric or magnetic particles are added in the manufacturing process, these structures can be tuned through remote fields to attain a specific mechanical behaviour. This promising technique has direct applications in high-impact fields such as bioengineering, soft robots or sensor designing. Filament-shaped smart sensors can send electrical signals when subjected to an external mechanical stimulus or provide a mechanical response when a remote and controllable field is applied broadening their possibilities of action. As the efficient design of these structures is highly challenging, developing a technical tool with a low computational cost to help throughout layout processes (i.e. inverse engineering) is pivotal. Theoretical modelling of the kinematics and dynamics of a wire-shaped structure under an external action is the first step to provide a methodology to help designing mechanical sensors in an efficient, understandable and low time-consuming way. The event of mechanical deformation after receiving the external stimulus and before sending the corresponding output signal is key in the conceptualisation process of smart sensors. This work intends to give insight into the dynamics of a deformable pillar-shaped sensor component under an external action without addressing or coupling its causes and, hence, provide the general mechanical framework to serve as basis for multiphysics formulations for pillar-shaped sensor design.

1. Introduction

Recent years have witnessed the development and expansion of bioinspired materials that can react to external stimuli. These materials are designed to mimic the optimal structures, behaviours and responses provided by nature over millennia of evolution. Several branches of research have arisen to leverage the key resources in nature to fulfill engineering needs in different domains. These new routes are reflected in on-going promising fields such as bioengineering (Bastola and Hossain, 2021; Moreno-Mateos et al., 2022, 2023), soft robotics (Wu et al., 2022; Wang et al., 2021) or sensor applications (Moreno-Mateos et al., 2022; Rambausek et al., 2022; Mukherjee and Danas, 2022; Garcia-Gonzalez et al., 2023; Perez-Garcia et al., 2024) to highlight a few. The fundamental concept behind the modelling of a structure, component or device sensitive to external stimuli is the addition of small particles reactive to external fields (i.e. electric, magnetic) that can be remotely controlled and modified to induce a desired response (Lopez-Donaire et al., 2023). Remote controlling of the mechanical behaviour through the application of external fields broadens the possibilities for these materials to be used in the design of bioinspired smart sensors for healthcare purposes (Zhang et al., 2019; Wang et al., 2021).

Smart mechanical actuators are adaptable to different approaches spanning from task-oriented functions of soft tissues in the human body to drug delivery. This versatility enhances the design of sensors that turn a physiological signal into an output for human activity monitoring (Cheng et al., 2020; Zhang et al., 2019). Specifically, soft materials based on mimicking filament-, rod-, wire-, pillar-shaped structures, found in biological systems, show the highest sensitivity to shear stresses (Zhao and Ahn, 2022). For instance, hairy systems in natural organisms can capture subtle airflows that alter the potential of the cells transmitting electrical signals to the nerves at the roots (Xiong et al., 2020; Wu et al., 2019; Zhang et al., 2016). Furthermore, fish possess mechanoreceptors that distinguish vibrations and flow movements and are used for swimming (Ilami et al., 2021; Wang et al., 2022a). Inspired by this concept, a tactile sensor based on conductive Au micro-pillars on a bottom layer of conductive polyaniline (PANI) was designed to detect forces in real time (Park et al., 2014). The

* Corresponding author.
E-mail addresses: alberto.solis@uca.es (A. Solis), luis.alonso.sanjose@urjc.es (L. Alonso).

https://doi.org/10.1016/j.mechmat.2024.105031
Received 28 February 2024; Received in revised form 15 April 2024; Accepted 5 May 2024
Available online 13 May 2024

detection of other external mechanical stimuli such as human breathe, forward and backward winds or music is another valuable asset of flexible slender structures. Another possibility for micro-pillar actuators is the shape-morphing phenomena (i.e. bending, coiling, elongation, deflection, etc.) through the application of external magnetic or electric fields to tune the mechanical movement to control and achieve a desired change of shape (Kiang et al., 2013; Zhao et al., 2018). These actuators can be effectively built with the aid of 3D and 4D printing processes to insert distributions of magnetic or electric microparticles that can react to external fields (Lopez-Donaire et al., 2023; Kim et al., 2018; Zhu et al., 2021). By alternating these fields, a wire or a functionalised beam can sway or bend in different directions (Lopez-Donaire et al., 2023; Shen et al., 2016). They can also change stiffness and mechanical deformation forming heterogeneous patterns coupling the change in electric conductivity with mechanical deformation. Complex or simple magnetic soft continuum robots (MSCRs) are composed by these conductive filaments. The functionality of microrods inspired by cilia and gecko toe hairs was controlled to design the magnetic legs of a millipede-inspired soft robot for drug delivery on different terrains and conditions (Lu et al., 2018). Long fibres can be manufactured to convert electric power in mechanical energy and thus serve as fundamental units of artificial muscles (Ilami et al., 2021; Wang et al., 2022b). In addition, passive guidewires made of elastomeric fibres have been proven to successfully prevent the formation of aneurysms by enhancing their steerability under remote magnetic fields (Wang et al., 2021). Overall, the use of filament-shaped structures is a current approach in the design of bioinspired smart sensors and actuators and thus the need for a proper mathematical modelling to give insight into their mechanical behaviour is required.

The understanding of the mechanical behaviour in the design of the above described pillar-shaped soft sensors and actuators in absence and presence of an external field constitutes a compelling reason to develop analytical models describing the kinematics and dynamics. The most common technique to predict the structural behaviour when conceptualising a sensor able to respond to external stimuli of any kind is either experimental or finite element approaches (Lopez-Donaire et al., 2023; Zhao and Ahn, 2022; Ilami et al., 2021). However, analytical models that can turn a force provoked by an external field into a movement that can be potentially associated to an electrical signal to monitor or act on a physiological process are a valuable tool. This is because they are less time consuming than FE models and experiments, help understanding the physics involved and can be efficiently applied to inverse engineering problems. Although this procedure is not the most common, a few analytical models are available: Wang et al. (2021) developed a finite difference scheme to predict the movement of guidewires and control them when subjected to a remote magnetic field to treat heart diseases.

In this work, a methodology to hand over the mechanical framework constituting the basis to support multiphysics formulations for the design of filament-shaped bioinspired smart sensors-actuators is presented. Through a non-dimensional formulation, the independent groups of the problem are revealed. As for the integro-differential governing equation, an approximation by means of a midpoint rule is used, being the derivatives expressed through a finite difference method (FDM) scheme. The original matrices conveniently defined to discretise the problem lead to a very compact formulation enabling accurate identification of the physical meaning of every term, which is key to use this methodology in inverse engineering applications. Furthermore, a FE model is implemented as a tool to validate the analytical formulation.

2. Theoretical development: Mechanistic description

In this section, the analytical formulation to describe the in-plane (2D) dynamic response of a continuous deformable pillar-shaped structure, also known as a wire, with bending rigidity is exposed. The so-called wire is subjected to a constant field understood as the gravitational force of the weight and is pinned in one of its ends because it is the most common boundary condition when designing these sensors/actuators. Note that wire should be interpreted as a 1D solid on the grounds that one of the dimensions is remarkably larger than the remaining two. At this point, several fundamental hypotheses are assumed throughout the problem formulation. The wire stiffness is infinite to axial efforts and is characterised as an inextensible solid in the axial direction. Moreover, the relevant dimension is parametrised by the arc length of the deformable line crossing all sections centroids. The cross-section is considered to be circular and always perpendicular to the arc length coordinate. The above description constitutes the basis of the 1D deformable wire definition hereinafter.

In the first subsection, the intrinsic framework and the kinematic relationships of the in-plane motion are obtained by defining the behaviour of a differential wire slice along the arc length coordinate under bending efforts. The second subsection aims to develop the particular 2D equilibrium expressions from the general 3D approach in a non-dimensional form for a differential slice to elucidate the integro-differential governing equation. A discretisation of the spatial domain is proposed in the third subsection to turn the continuous governing equation into a system that can be numerically solved in time. In the last subsection, both the continuous and discretised expressions are presented for the kinetic and potential energies as a part of data post-processing.

2.1. Local axes, kinematic relationships and constitutive law

Conceiving the wire as a sensor or actuator whose mission is to translate a movement into signals or reply with motion to a stimulus received, it is highly recommended to use a local framework to express the physical quantities of the problem given the change in the relative position of a differential element within the wire as this motion evolves. An intrinsic Frenet trihedron parametrised through the arc length of the wire, s, is accordingly defined providing each wire element position, $\vec{r}(s,t)$, with local axes fixed to it. An schematic representation of this local framework is shown in Fig. 1(a).

The first reference vector tangent to the arc length coordinate is defined in Eq. (1a). Furthermore, $ds = |d\vec{r}|$ by definition, hence $\vec{T}(s,t)$ turns out to be normalised. This parametrisation is well-known as *natural*. The second vector $\vec{N}(s,t)$ is defined counterclockwise perpendicular[1] to $\vec{T}(s,t)$ (see Eq. (1b)). Finally, the third vector closing the right-handed trihedron is perpendicular to the previous two and named binormal, $\vec{B}(s,t)$, through the cross product shown in Eq. (1c).

$$\vec{T}(s,t) = \frac{\partial \vec{r}(s,t)}{\partial s}, \tag{1a}$$

$$\vec{N}(s,t) \cdot \left| \frac{\partial \vec{T}(s,t)}{\partial s} \right| = \frac{\partial \vec{T}(s,t)}{\partial s}, \tag{1b}$$

$$\vec{B}(s,t) = \vec{T}(s,t) \times \vec{N}(s,t). \tag{1c}$$

Since motion is restricted to be in the $X-Y$ plane (see Fig. 1(a)), $\vec{B}$ results to be constant. This condition allows to consider the bending component alone contained in the motion plane. As it can be derived from Fig. 1(a), the relationships relating the inertial and Frenet axes are functions of the angle enclosed by $\vec{T}(s,t)$ and the canonical vector, $\vec{j}$, named $\theta(s,t)$. This angle accounts for the relative inclination of the wire element with respect to $\vec{j}$. The plane rotation of the Frenet axes with respect to the canonical vectors are expressed as

$$\begin{bmatrix} \vec{T}(s,t) \\ \vec{N}(s,t) \end{bmatrix} = \begin{bmatrix} \sin\theta(s,t) & \cos\theta(s,t) \\ \cos\theta(s,t) & -\sin\theta(s,t) \end{bmatrix} \cdot \begin{bmatrix} \vec{i} \\ \vec{j} \end{bmatrix}. \tag{2}$$

[1] Note that by deriving $\vec{T}(s,t)\cdot\vec{T}(s,t) = 1$ with respect to s, $\vec{T}(s,t)\cdot\frac{\partial \vec{T}(s,t)}{\partial s} = 0$, proving the perpendicularity between both intrinsic vectors.

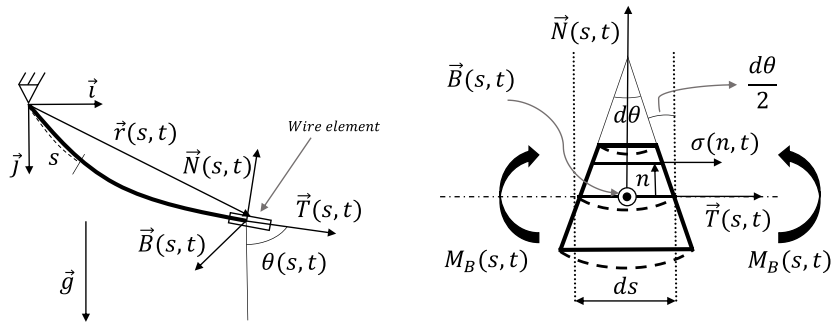

(a) Frenet trihedron defined at $\vec{r}(s,t)$ *(b) Differential wire slice under bending*

Fig. 1. Definition of the local framework for a differential wire slice.

Derivation of $\vec{T}(s,t)$ and $\vec{N}(s,t)$ with respect to time combined with Eq. (2) hands over the following relationships

$$\dot{\vec{T}}(s,t) = \dot{\theta}(s,t)\vec{N}(s,t), \tag{3a}$$

$$\dot{\vec{N}}(s,t) = -\dot{\theta}(s,t)\vec{T}(s,t). \tag{3b}$$

Eqs. (3a) and (3b) are particularisations of the Frenet–Serret formulas for plane motion multiplied by $\dot{s}$. Even though intrinsic axes have been already used to describe the local motion of thin liquid jets in air (Entov and Yarin, 1984), some numerical instabilities have been reported (Ribe, 2004) in these cases. In spite of that, the plane dynamics of a material wire yields stable results using this formulation. The second derivative with respect to time of the tangent vector is procured from Eqs. (3)

$$\ddot{\vec{T}}(s,t) = \ddot{\theta}(s,t)\vec{N}(s,t) - \dot{\theta}^2(s,t)\vec{T}(s,t). \tag{4}$$

Then, integration of Eq. (1a) with respect to the arc length coordinate and derivation two times with respect to time leads to an expression of the wire element acceleration

$$\ddot{\vec{r}}(s,t) = \int_0^s \left[\ddot{\theta}(s',t)\vec{N}(s',t) - \dot{\theta}^2(s',t)\vec{T}(s',t)\right] ds', \tag{5}$$

where the term on the right hand side has been obtained by substituting Eq. (4). Lastly, the constitutive law of a wire differential slice relates the bending internal effort $M_B(s,t)$[2] to the curvature of the wire at each s coordinate. Note that every material fibre is assumed to be straight in agreement with small strains hypothesis yet the wire directrix is perpendicular to each cross-section. In favour of establishing the constitutive wire behaviour between longitudinal strain, $\epsilon(n,t)$, and stress, $\sigma(n,t)$, a 1D Hooke law is used for simplicity although any other law according to the behaviour of the specific sensor designed could be chosen.[3] The longitudinal strain of the slice can be inferred from Fig. 1(b): on the one hand, small strains hypothesis brings out the approximation consisting for $\epsilon(n,t)$ to be $-n \cdot d\theta(n,t)/ds$.[4] On the other hand, the Young's modulus of the wire material, E, is the constant of proportionality relating stresses to strains. Moreover, the binormal component of the internal torque, $M_B(s,t)$, is taken as the integral extended to the cross-section area of the momentum generated by $\sigma(n,t)$, preceded by minus sign,[5] with respect to the centroid. Taking all these aspects into account, the constitutive law for the wire slice is determined

$$M_B(s,t) = EI\frac{d\theta(s,t)}{ds}, \tag{6a}$$

$$I = \int_A n^2 dA. \tag{6b}$$

Note that Eq. (6b) describes the slice static inertia, I, with respect to the direction of the binormal vector perpendicular to the motion plane and A is the circular cross-section area. As already stated, the previous reasoning provides a well-known result for unidimensional beams establishing bending to be proportional to the curvature of the wire directrix.

2.2. Dynamic equations of motion

In this subsection, in-plane equations of motion are established from the complete relationships of the 3D case. These equations are handed over from the dynamic equilibrium of a differential wire slice of length, ds, circular constant cross-section area, A, and volumetric density, ρ, represented in Fig. 2. As shown in Fig. 2(a), the position of a slice material point is given by the vector $\vec{r}(s,t) + \vec{y}(s,t)$, where $\vec{r}(s,t)$ defines the position of the centroid, G, and $\vec{y}(s,t)$ is a vector from G to the material point.[6] In Fig. 2, each Frenet trihedron, attached to and moving with the slice, is animated with a translation velocity, $\dot{\vec{r}}(s,t)$, and an angular velocity, $\vec{\omega}(t)$, with respect to inertial axes to simulate the movement of the sensor/actuator during its performance.

Additionally, the internal effort and torque of the differential slice are represented by $\vec{R}(s,t)$ and $\vec{M}(s,t)$ vectors, respectively (see Fig. 2(b)). These vectors are functions of the arc length coordinate and first order variations are considered. In this condition, the kinetic momentum of the slice, $\vec{\Gamma}_G$, with respect to the centroid can be expressed as

$$\vec{\Gamma}_G = \rho ds\left[\int_A \vec{y}(s,t)\times\vec{\omega}(t)\times\vec{y}(s,t)dA + \int_A \vec{y}(s,t)dA\times\dot{\vec{r}}(s,t)\right]. \tag{7}$$

Note that the second integral is null due to G is the origin of the Frenet trihedron as already stated. The following definition is also made for the circular wire cross-section

$$J = \int_A \left(n^2+b^2\right)dA = 2\int_A b^2 dA = 2I = \frac{A^2}{2\pi}, \tag{8}$$

where J is the polar inertia and the nonentity of product of inertia must be noted, yet the cross-section is circular. Through the use of Eq. (8), the kinetic momentum results in[7]

$$\vec{\Gamma}_G = \rho I ds\left[\vec{B}(s,t)\times\dot{\vec{B}}(s,t) + \vec{N}(s,t)\times\dot{\vec{N}}(s,t)\right]. \tag{9}$$

[2] In this context, $M_B(s,t)$ represents the internal torque component in the direction of the binormal intrinsic vector $\vec{B}(s,t)$.

[3] The coordinate n is addressed along the local axis $\vec{N}(s,t)$ (see Fig. 1(b)).

[4] The minus sign implies curtailment of the material fibre in positive coordinates (see Fig. 1(b)).

[5] Representing for the bending effort to be counterclockwise in the right slice face. The local framework is precisely centred in the section centroid.

[6] The local vector components are $\vec{y}(s,t) = n\vec{N}(s,t) + b\vec{B}(s,t)$.

[7] The equality is established by considering the Poisson formula to derive a non-inertial referential frame vector $\dot{\vec{v}} = \vec{\omega}(t)\times\vec{v}$.

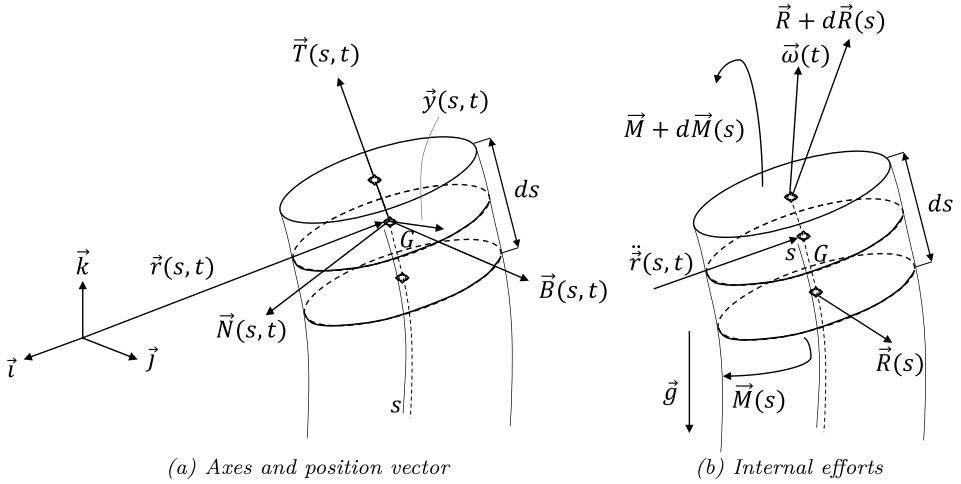

(a) Axes and position vector *(b) Internal efforts*

Fig. 2. Geometry and internal efforts of a differential wire slice. The Frenet trihedron is fixed to the centroid of the section, G, and is animated with an angular velocity, $\vec{\omega}(t)$, with respect to inertial axes. The position vector of any slice material point is $\vec{r}(s,t)+\vec{y}(s,t)$.

By applying the dynamic equilibrium of forces and momentum to the differential slice represented in Fig. 2(b) and simplifying and dividing by ds, the following expressions are obtained

$$\frac{d\vec{R}(s,t)}{ds}+\lambda\vec{g}=\lambda\ddot{\vec{r}}(s,t), \tag{10a}$$

$$\frac{d\vec{M}(s,t)}{ds}+\vec{T}(s,t)\times\vec{R}(s,t)=\rho I\left[\vec{B}(s,t)\times\ddot{\vec{B}}(s,t)+\vec{N}(s,t)\times\ddot{\vec{N}}(s,t)\right]. \tag{10b}$$

The term on the right hand side of Eq. (10b) appears when deriving Eq. (9) with respect to time and $\lambda=\rho A$ is the wire lineal density. Eqs. (10a) and (10b) govern the translational and rotational motion of a wire differential slice. An equivalent formulation has been used to successfully describe the coiling of flexible ropes (Mahadevan and Keller, 1996) and viscous jets (Ribe, 2004). The particularisation of Eqs. (10a) and (10b) for plane motion can be achieved by considering $\vec{R}(s,t)$, $\vec{g}$ and $\ddot{\vec{r}}(s,t)$ vectors to be restricted to $X-Y$ plane, multiplying the constant vector $\vec{B}$ by Eq. (10b)[8] and substituting Eq. (6a). Moreover, integration of Eq. (10a) from s to the wire length, L, subjected to a free end boundary condition, $\vec{R}(L,t)=0$, with previous substitution of Eq. (5) in Eq. (10a), provides the internal effort $\vec{R}(s,t)$. Thus, Eqs. (10) are rewritten as

$$\vec{R}(s,t)=\lambda\left[\vec{g}\int_s^L ds'-\int_s^L\int_0^{s'}\left[\ddot{\theta}(s'',t)\vec{N}(s'',t)-\dot{\theta}^2(s'',t)\vec{T}(s'',t)\right]ds''ds'\right], \tag{11a}$$

$$EI\frac{d^2\theta(s,t)}{ds^2}+\vec{R}(s,t)\cdot\vec{N}(s,t)=-\rho I\left(\ddot{\vec{N}}(s,t)\cdot\vec{T}(s,t)\right). \tag{11b}$$

Considering the arrangement in the canonical basis that Eq. (2) provides for the scalar products of intrinsic vectors[9] and the substitution of Eq. (11a) in Eq. (11b), leads to the governing equation of the problem

$$\frac{EI}{\lambda}\frac{d^2\theta(s,t)}{ds^2}+g\sin\big(\theta_g-\theta(s,t)\big)(L-s)-\int_s^L\int_0^{s'}\big[\cos\big(\theta(s'',t)-\theta(s,t)\big)\ddot{\theta}(s'',t)-\sin\big(\theta(s'',t)-\theta(s,t)\big)\dot{\theta}^2(s'',t)\big]ds''ds'=-\frac{\rho I}{\lambda}\left(\ddot{\vec{N}}(s,t)\cdot\vec{T}(s,t)\right). \tag{12}$$

As shown, θ_g represents the possibility of gravity inclination with respect to $\vec{j}$ in Eq. (12). To attain a non-dimensional formulation, the following relationships are required

$$\bar{s}L=s;\ \ \bar{t}=\omega t\ \ (\omega^2\lambda L^4=EI);\ \ \bar{g}\omega^2L=g, \tag{13}$$

where bars indicate non-dimensionality. In this regard, Eq. (12) is rewritten to address the previous non-dimensional formulation as

$$\frac{d^2\theta\left(\bar{s},\bar{t}\right)}{d\bar{s}^2}+\bar{g}\sin\left(\theta_g-\theta\left(\bar{s},\bar{t}\right)\right)(1-\bar{s})-\int_{\bar{s}}^1\int_0^{\bar{s}'}\left[\cos\left(\theta\left(\bar{s}'',\bar{t}\right)-\theta\left(\bar{s},\bar{t}\right)\right)\ddot{\theta}\left(\bar{s}'',\bar{t}\right)-\sin\left(\theta\left(\bar{s}'',\bar{t}\right)-\theta\left(\bar{s},\bar{t}\right)\right)\dot{\theta}^2\left(\bar{s}'',\bar{t}\right)\right]d\bar{s}''d\bar{s}'=-\frac{\rho I}{\lambda L^2}\left(\ddot{\vec{N}}\left(\bar{s},\bar{t}\right)\cdot\vec{T}\left(\bar{s},\bar{t}\right)\right). \tag{14}$$

Additional considerations for the term on the right hand side of Eq. (14) can be made. Given that $\frac{\rho I}{\lambda L^2}=\frac{I}{AL^2}\sim\frac{A}{L^2}$ (see Eq. (8)), the rotational inertia of the slice results to be negligible compared to the other terms of unit order, in virtue of the wire slenderness $A\ll L^2$. Therefore, neglecting the referred term seems a reasonable assumption, simplifying Eq. (14) to

$$\frac{d^2\theta\left(\bar{s},\bar{t}\right)}{d\bar{s}^2}=\int_{\bar{s}}^1\int_0^{\bar{s}'}\left[\cos\left(\theta(\bar{s}'',\bar{t})-\theta\left(\bar{s},\bar{t}\right)\right)\ddot{\theta}\left(\bar{s}'',\bar{t}\right)-\sin\left(\theta(\bar{s}'',\bar{t})-\theta\left(\bar{s},\bar{t}\right)\right)\dot{\theta}^2\left(\bar{s}'',\bar{t}\right)\right]d\bar{s}''d\bar{s}'-\bar{g}\sin\left(\theta_g-\theta\left(\bar{s},\bar{t}\right)\right)(1-\bar{s}). \tag{15}$$

2.3. Spatial discretisation

Solving Eq. (15) requires to discretise the spatial domain of the pillar-shaped structure, $\bar{s}$. To meet this objective, the wire length is considered to be splitted into N discrete partitions of dimensionless magnitude $\frac{1}{N}$. These discrete partitions are directly correlated to the continuum differential slices, being the discrete version of them. Consequently, the arc length becomes $\bar{s}_i$, meaning i the actual discrete position considered to be located at the centre of each interval (see Fig. 3):

With such discretisation, the term $(1-\bar{s})$ of Eq. (15) becomes $\frac{N-i+\frac{1}{2}}{N}$. Analogously, the field $\theta(\bar{s},\bar{t})$ discretises as $\theta_i\left(\bar{t}\right)$ and the integrals can be approximated through a midpoint rule by choosing appropriate indices in the summaries. The second derivative in the term on the left hand

[8] To simplify, note that $\vec{B}\cdot\vec{M}(s,t)=M_B(s,t)$. Also, the triple products can be transformed by circular shifting as follows: $\vec{B}\cdot\left(\vec{T}\times\vec{R}\right)=\vec{R}\cdot\vec{N}$, $\vec{B}\cdot(\vec{B}\times\ddot{\vec{B}})=0$ and $\vec{B}\cdot(\vec{N}\times\ddot{\vec{N}})=-\ddot{\vec{N}}\cdot\vec{T}$.

[9] For instance, $\vec{T}(s'',t)\cdot\vec{N}(s,t)=\sin\theta(s'',t)\cos\theta(s,t)-\cos\theta(s'',t)\sin\theta(s,t)=\sin\big(\theta(s'',t)-\theta(s,t)\big)$.

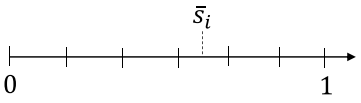

Fig. 3. Spatial discretisation of the arc length coordinate.

side is likewise estimated by a centred difference scheme[10], assuming errors of $\sim O\left(\frac{1}{N^2}\right)$. For all the stated above, Eq. (15), maintaining the time dependency, becomes

$$\begin{aligned}&\left[\sum_{k=i}^{k=N}\gamma_{ik}\sum_{j=1}^{j=k}\xi_{kj}\cos\left(\theta_j\left(\bar{t}\right)-\theta_i\left(\bar{t}\right)\right)\ddot{\theta}_j\left(\bar{t}\right)\right]\\&=\left[\sum_{k=i}^{k=N}\gamma_{ik}\sum_{j=1}^{j=k}\xi_{kj}\sin\left(\theta_j\left(\bar{t}\right)-\theta_i\left(\bar{t}\right)\right)\dot{\theta}_j^2\left(\bar{t}\right)\right]\\&+N^2\left(\theta_{i+1}\left(\bar{t}\right)-2\theta_i\left(\bar{t}\right)+\theta_{i-1}\left(\bar{t}\right)\right)+\frac{\bar{g}}{N}\sin\left(\theta_g-\theta_i\left(\bar{t}\right)\right)\left(N-i+\frac{1}{2}\right).\end{aligned}\tag{16}$$

Note that i index is free, meaning that Eq. (16) corresponds to each i partition. When $k=i$ or $j=k$, γ_{ik} and ξ_{kj} tensors are respectively equal to $\frac{1}{2N}$ due to the centred position of $\bar{s}_i$ in the discrete partition (see Fig. 3) which only implies half width of the interval. However, they have to be equal to $\frac{1}{N}$ if $k>i$ or $j<k$. To enable a compact and efficient matrix treatment of Eq. (16), additional null terms could be added to the summaries to make the matrices dimensions equal. This can be addressed expanding the indices from 1 to N in all summaries. Thus, $k<i$ and $j>k$ imply null values for γ_{ik} and ξ_{kj} respectively, in these cases, hereinafter. According to these vicissitudes, the following matrices and vectors are defined

$$C_{ij}\left(\bar{t}\right)=\begin{cases}\left(\frac{1}{2}+N-i\right)\cos\left(\theta_j\left(\bar{t}\right)-\theta_i\left(\bar{t}\right)\right); & if\ \ (j<i)\\ \frac{1}{4}+N-i; & if\ \ (j=i)\\ \left(\frac{1}{2}+N-j\right)\cos\left(\theta_j\left(\bar{t}\right)-\theta_i\left(\bar{t}\right)\right); & if\ \ (j>i),\end{cases}\tag{17a}$$

$$S_{ij}\left(\bar{t}\right)=\begin{cases}\left(\frac{1}{2}+N-i\right)\sin\left(\theta_j\left(\bar{t}\right)-\theta_i\left(\bar{t}\right)\right); & if\ \ (j<i)\\ 0; & if\ \ (j=i)\\ \left(\frac{1}{2}+N-j\right)\sin\left(\theta_j\left(\bar{t}\right)-\theta_i\left(\bar{t}\right)\right); & if\ \ (j>i),\end{cases}\tag{17b}$$

$$K_{ij}=\begin{cases}1; & if\ \ (j=i-1)\\ -2; & if\ \ (j=i)\\ 1; & if\ \ (j=i+1)\\ 0; & otherwise,\end{cases}\tag{17c}$$

$$F_i\left(\bar{t}\right)=\sin\left(\theta_g-\theta_i\left(\bar{t}\right)\right)\left(N-i+\frac{1}{2}\right).\tag{17d}$$

Index notation is recalled to express Eq. (16) in a more compact form[11]:

$$\begin{aligned}&C_{ij}\left(\bar{t}\right)\ddot{\theta}_j\left(\bar{t}\right)=S_{ij}\left(\bar{t}\right)\dot{\theta}_j^2\left(\bar{t}\right)+N^4K_{ij}\theta_j\left(\bar{t}\right)+\bar{g}NF_i\left(\bar{t}\right),\\&\theta_j(0)=\theta_{oj},\\&\dot{\theta}_j(0)=\dot{\theta}_{oj}.\end{aligned}\tag{18}$$

In this context, $\theta_j\left(\bar{t}\right)$ vector contains the counterclockwise inclination angle of each j partition with respect to $\vec{j}$ at every instant $\bar{t}$ (see Fig. 1(a)) and $\dot{\theta}_j\left(\bar{t}\right)$ is its derivative with respect to time. The second order initial value problem (IVP) given by the $N\times N$ system described by Eqs. (18) and its initial conditions governs the in-plane motion of a 1D wire subjected to an impulsive signal represented by the initial conditions (θ_{oj} and $\dot{\theta}_{oj}$ are the initial values of the inclination angles and angular velocities of each partition) given in Eq. (18). This discretisation of the spatial domain can be usually solved in time using a Runge–Kutta method after transforming it into a double-size system of first order.

As said, the formulation presented in Eqs. (18) addresses the 2D dynamic response of a deformable inextensible wire subjected to a constant gravity field. However, in cases subjected to non-constant fields, the formulation must be properly modified. If the external fields are known, they can be integrated into the formulation by discretising their field equations properly. It is important to distinguish between time or space dependence. While time dependence can be taken into account in the appropriate term in Eqs. (18), by updating the amplitude at every instant, dependencies involving spatial derivatives may require finite difference schemes, similar to those used for the curvature in this work. Some examples are discussed for the magnetic torque in Ilami et al. (2021) or (Lopez-Donaire et al., 2023). These dependencies must be implemented by modifying the last term in the right-hand side of Eqs. (18) by including the proper discretisation and the variations in the known external field. Therefore, the first case requires computationally updating the amplitude of the field with known data, while space dependencies may modify the resultant algebraic IVP with additional terms from the derivatives discretisation.

2.4. Energy calculation

Calculating kinetic and potential energies over the wire motion is an enriching and enlightening task from a physical interpretation point of view. In behalf of the nature of the problem, energies are obtained once the positions and velocities of the wire elements are available as a post-processing assignment. Knowing the position vector and its derivatives is a consequence of the accessibility of $\theta_j\left(\bar{t}\right)$ and $\dot{\theta}_j\left(\bar{t}\right)$ at every instant of time. Keeping this in mind, the total kinetic energy of the wire over time, $T(t)$, is defined through the following integration:

$$\begin{aligned}T(t)&=\frac{1}{2}\lambda\int_0^L\dot{\vec{r}}(s,t)\cdot\dot{\vec{r}}(s,t)ds\\&=\frac{1}{2}\lambda\int_0^L\int_0^s\int_0^s\cos\left(\theta(s'',t)-\theta(s',t)\right)\dot{\theta}(s'',t)\dot{\theta}(s',t)ds''ds'ds,\end{aligned}\tag{19}$$

where Eqs. (1a) and (3a) have been used to figure out the velocity of each wire element projected in the intrinsic framework. In addition, the scalar product of intrinsic vectors is set in agreement with the previous reasoning based on the transformations given in Eq. (2). Thus, using the non-dimensional normalisation (see Eqs. (13)), the kinetic energy is discretised as

$$\begin{aligned}\bar{T}\left(\bar{t}\right)&=\frac{T(t)L}{EI}\\&=\frac{1}{2}\int_0^1\left[\int_0^{\bar{s}}\int_0^{\bar{s}}\cos\left(\theta\left(\bar{s}'',\bar{t}\right)-\theta\left(\bar{s}',\bar{t}\right)\right)\dot{\theta}\left(\bar{s}'',\bar{t}\right)\dot{\theta}\left(\bar{s}',\bar{t}\right)d\bar{s}''d\bar{s}'\right]d\bar{s}\\&\approx\frac{1}{2}\sum_{k=1}^{k=N}\frac{1}{N}\sum_{i=1}^{i=k}\xi_{ki}\sum_{j=1}^{j=k}\xi_{kj}\cos\left(\theta_j\left(\bar{t}\right)-\theta_i\left(\bar{t}\right)\right)\dot{\theta}_j\left(\bar{t}\right)\dot{\theta}_i\left(\bar{t}\right)\\&=\frac{1}{2N^3}\dot{\theta}_i\left(\bar{t}\right)C_{ij}\left(\bar{t}\right)\dot{\theta}_j\left(\bar{t}\right).\end{aligned}\tag{20}$$

The matrix $C_{ij}\left(\bar{t}\right)$ (see Eq. (17a)) is elected[12] to express $\bar{T}\left(\bar{t}\right)$ as a quadratic form of $\dot{\theta}_i\left(\bar{t}\right)$, which can be computed after solving Eqs. (18).

Analogously, the gravitational potential energy $V_g(t)$ can be written as

$$V_g(t)=-\lambda\int_0^L\vec{g}\cdot\vec{r}(s,t)ds=-\lambda\int_0^L\int_0^s g\cos\left(\theta_g-\theta(s',t)\right)ds'ds.\tag{21}$$

[10] Meaning that $\frac{d^2\theta(\bar{s},\bar{t})}{d\bar{s}^2}\rightarrow\frac{\left(\theta_{i+1}(\bar{t})-2\theta_i(\bar{t})+\theta_{i-1}(\bar{t})\right)}{1/N^2}+O\left(\frac{1}{N^2}\right)$.

[11] In Einstein notation, repeated indices imply summation. Additionally, in Eqs. (18), $i,j=1,\ldots,N$.

[12] Note that $\sum_{i=1}^{i=k}\xi_{ki}\sum_{j=1}^{j=k}\xi_{kj}f_{ij}\left(\bar{t}\right)=\sum_{i=1}^{i=k}\gamma_{ik}\sum_{j=1}^{j=k}\xi_{kj}f_{ij}\left(\bar{t}\right)$ where $f_{ij}\left(\bar{t}\right)=\cos\left(\theta_j\left(\bar{t}\right)-\theta_i\left(\bar{t}\right)\right)\dot{\theta}_j\left(\bar{t}\right)\dot{\theta}_i\left(\bar{t}\right)$.

The last term of Eq. (21) is procured through Eqs. (1a), (3a) and (2). The expression given in Eq. (21) can be also rewritten in its non-dimensional form and discretised using the same variables and tensors presented above

$$\begin{aligned}\bar{V}_g\left(\bar{t}\right) &= \frac{V_g(t)L}{EI} = -\bar{g}\int_0^1\int_0^{\bar{s}}\cos\left(\theta_g-\theta\left(\bar{s}',\bar{t}\right)\right)d\bar{s}'d\bar{s}\\ &\approx -\bar{g}\sum_{k=1}^{k=N}\frac{1}{N}\sum_{i=1}^{i=k}\xi_{ki}\cos\left(\theta_g-\theta_i\left(\bar{t}\right)\right)\\ &= -\frac{\bar{g}}{N^2}\sum_{k=1}^{k=N}\left(\frac{1}{2}+(N-k)\right)\cos\left(\theta_g-\theta_k\left(\bar{t}\right)\right).\end{aligned} \tag{22}$$

Given the relative character of gravitational potential energy, it is convenient to define an arbitrary origin for potential values. In this sense, a proper reference state would be the one of the extended wire in the direction of gravity ($\theta_g = \theta_k(\bar{t})$ for $k = 1, 2, \ldots, N$). Substituting in Eq. (22)[13]

$$\bar{V}_{og} = -\frac{\bar{g}}{N^2}\sum_{k=1}^{k=N}\left(\frac{1}{2}+(N-k)\right) = -\frac{\bar{g}}{N^2}\left(\frac{N}{2}+N^2-\frac{N(N+1)}{2}\right) = -\frac{\bar{g}}{2}. \tag{23}$$

Through this result, gravitational potential variations can be expressed using Eq. (23) as $\bar{V}_g\left(\bar{t}\right) - \bar{V}_{og}$.

Finally, the internal strain energy, $V_e(t)$, is formulated by integrating the product of the internal torque by the curvature of the wire along the arc length coordinate

$$V_e(t) = \int_0^L M_B(s,t)\frac{d\theta(s,t)}{ds}ds = EI\int_0^L\left(\frac{d\theta(s,t)}{ds}\right)^2 ds. \tag{24}$$

Be aware that Eq. (6a) has allowed to substitute $M_B(s,t)$ as a function of curvature. Following the same process displayed above Eq. (25) is obtained

$$\begin{aligned}\bar{V}_e(\bar{t}) = \frac{V_e(t)L}{EI} &= \int_0^1\left(\frac{d\theta\left(\bar{s},\bar{t}\right)}{d\bar{s}}\right)^2 d\bar{s} \approx \frac{N}{4}\sum_{i=2}^{i=N-1}\left(\theta_{i+1}\left(\bar{t}\right)-\theta_{i-1}\left(\bar{t}\right)\right)^2\\ &+ N\left(\theta_2(\bar{t})-\theta_1(\bar{t})\right)^2 + N\left(\theta_N(\bar{t})-\theta_{N-1}(\bar{t})\right)^2.\end{aligned} \tag{25}$$

As shown, the curvature is estimated by a centred difference scheme[14] from second to $N-1th$ partition while the forward and backward formulas[15] are used for the first and last partition, respectively. These approximations involve errors in the addends of $\sim O\left(\frac{1}{N^2}\right)$ and $\sim O\left(\frac{1}{N}\right)$.

3. Validation method: Finite element approach

3.1. Set-up of the finite element model

The mechanistic model described in the last section enables physical interpretation through the different mathematical terms involved in the formulation. This understanding gives insight into the qualitative behaviour of a pillar-shaped structure, providing a tool for calibrating or choosing a material for a specific sensor or actuator oriented to a precise application. This study is meant to constitute a handy tool to help designing bioinspired smart sensors or actuators. Hence, assessing the accuracy of this approach and the reliability of the hypotheses assumed is the aim of this section. Due to the lack of experimental resources, a FE approach, which is an extended, common and well-established technique that offers a reliable framework for the analysis of mechanical problems, is elected for the validation of the predicted wire dynamics.

Table 1
Summary of the wire properties used in the FE simulations.

Property	Nomenclature	Value
Volumetric density	ρ	280 kg/m^3
Length	L	0.1 m
Gravity	g	9.81 m/s^2
Young's modulus	E	7.2 GPa
Π group of $\bar{g}$	$\bar{g}$	200
Radius	R	2.76 μm

A fundamental obstacle that arises when using both formulations is the dimensional and non-dimensional nature of the FE and analytical models, respectively. To address this problematic, the FE model needs to be built with dimensional values, ensuring at least that the non-dimensional groups present in the simplified analytical model, defined in Eqs. (13), do not vary to consistently correlate both models. Since the unique non-dimensional parameter which the analytical solution depends on is $\bar{g}$ (see Eqs. (18)), the number of parameters to be defined in the FE model is four according to the Vaschy-Buckingham theorem on the grounds that there are three independent magnitudes governing the problem: mass, length and time. Thus, if a circular sectional area is considered in the FE model, the required inputs for the wire are: section radius, R, wire length, L, Young's modulus, E, density, ρ and gravity, g. Since the section radius and length are related through the 1D wire hypothesis, $\frac{R}{L} \ll 1$, that makes a total of four parameters.

Based on the arguments given above, a convenient methodology to prepare an equivalent FE simulation is defined as follows. A value is fixed for the non-dimensional group ($\bar{g} = 200$) to run the simulations with the analytical model. In the FE model, all the parameters (ρ, L, g, E) are defined except for the radius, R, as Table 1 shows. With all these parameters defined, the radius for the FE model is obtained with Eq. (13) and $\bar{g} = 200$ so the non-dimensional groups are equal and the problems are equivalent:

$$R = \sqrt{\frac{4\rho L^3 g}{\bar{g}E}}. \tag{26}$$

All the values used hereinafter in the FE simulations are collected in Table 1.

3.2. Description of the finite element model

The model is formulated for dynamic analysis and explicit integration and is coded in Ansys/LS-Dyna. 1D Lagrangian elements were used to perform the simulations. Specifically, BEAM161 elements were selected with one integration point along length an four integration points in the cross section. The domain of each element is delimited by two nodes and an assistant node in the middle of the element with the only purpose of accounting for the orientation of the cross section. At each node three spatial displacements are available, making a total of six degrees of freedom (DOFs) per element. Due to the consideration of transverse shear strains by these elements, the transverse shear correction factor was set at the default value, which is $\frac{5}{6}$. A linear-elastic material model was used with the material constants collected in Table 1. A total of ten elements were used in all simulations hereinafter for both models. Furthermore, all displacements of node 0 were restrained and an initial angular velocity, $\dot{\theta}_{oi}$, together with an angle with respect to the vertical axis, θ_{oi}, were set for each element ($i = 1, 2, \ldots, 10$). The angular velocity can be understood as the effect caused by an external punctual input or signal that triggers the movement of the sensor as a handy first-order approximation. In this way, the model is fed with an initial condition simulating the external action and the subsequent mechanical response. Fig. 4 shows a schematic representation of a 1D continuous wire discretisation subjected to gravity with its initial conditions caused by an external action.

[13] Taking into account that $\sum_{k=1}^{k=N} k = \frac{N(N+1)}{2}$.

[14] Which is $\frac{d\theta(\bar{s},\bar{t})}{d\bar{s}} \rightarrow \frac{\theta_{i+1}(\bar{t})-\theta_{i-1}(\bar{t})}{2/N}$.

[15] These formulas are $N\left(\theta_2\left(\bar{t}\right)-\theta_1\left(\bar{t}\right)\right)$ and $N\left(\theta_N\left(\bar{t}\right)-\theta_{N-1}\left(\bar{t}\right)\right)$.

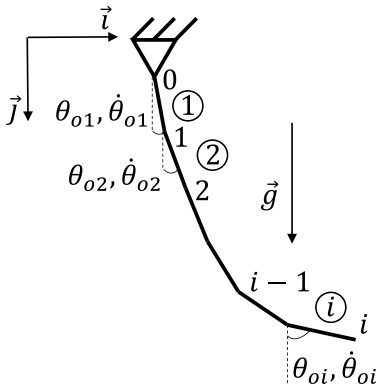

Fig. 4. Schematic representation of a 1D continuous wire discretisation subjected to gravity with initial conditions provoked by external actions. Nodes and elements are represented with numbers and circled numbers.

3.3. Validation of the analytical model

A reasonable methodology to perceive whether the analytical model captures with an acceptable accurateness the movement of a filament-shaped structure under an external punctual signal is the study of its movement. The wire dynamics predicted by the analytical model can be validated through the spatial coordinates of the nodes wherewith the remaining dynamic variables are derived from. Thus, the evolution over time of the two independent spatial coordinates seems to be a reliable comparison between the FE and analytical model. For the sake of clarity, only four equally spaced nodes are chosen to be represented in the subsequent analyses. In addition, the portrayal of the wire position over time is a visual and qualitative indicator of accurateness. The time scale used in the following simulations is defined according to the time that takes for the majority of the wire nodes to complete a full oscillation. Although the nodes have different periods, the deviations are negligible for small oscillations. Keeping this in mind, three configurations are studied varying the initial conditions. Figs. 5(a) and 5(b) show the analytical and FE predictions of the X and Y spatial coordinates of the four selected nodes, respectively, over time for a wire with initial conditions of $\theta_{oi} = 0$, $\dot{\theta}_{oi} = 1$ rad/s for all elements. Fig. 5(c) describes the position of the nodes within the $X - Y$ plane at 0.13 s, 0.25 s and 0.35 s.

Figs. 5(a) and 5(b) reflect an excellent agreement between the analytical and FE predictions for nodes 1, 4 and 7. Looking at node 10, the correlation is to some degree worse for the spatial X-coordinate compared to the spatial Y-coordinate, with a maximum difference of 4.4% between both models. Note that the oscillation of the wire is quite small as shown in Fig. 5(c). Hence, Fig. 5(b) does not provide much valuable information due to the unnoticeable Y-deviation of the nodes with respect to their initial position. Nonetheless, the initial conditions in Fig. 6 which are $\theta_{oi} = 0$, $\dot{\theta}_{oi} = 3$ rad/s for all elements, are more opportune to grade the spatial Y-coordinate predictions.

The trend observed in Figs. 5(a) and 5(b) is maintained in Figs. 6(a) and 6(b). Spatial X and Y-coordinates present an almost perfect resemblance between both models even though the maximum differences are still found for the spatial X-coordinate in node 10, being the largest variation 4.5%. This discrepancy results in a slightly variation in the wire curvature as Fig. 6(c) exposes. At last, simulations were performed to see if the analytical model achieves good predictions for larger oscillations. The initial conditions in Fig. 7 are $\theta_{oi} = 0$, $\dot{\theta}_{oi} = 5$ rad/s for all elements.

Fig. 7 exhibits the same behaviour than Fig. 6. The maximum differences are still found in node 10 for the spatial X-coordinate (4.7%). This discrepancy along with the excellent fitting displayed by the other nodes in Figs. 7(a) and 7(b) results in a slightly variance in the curvature of the wire as shown in Fig. 7(c).

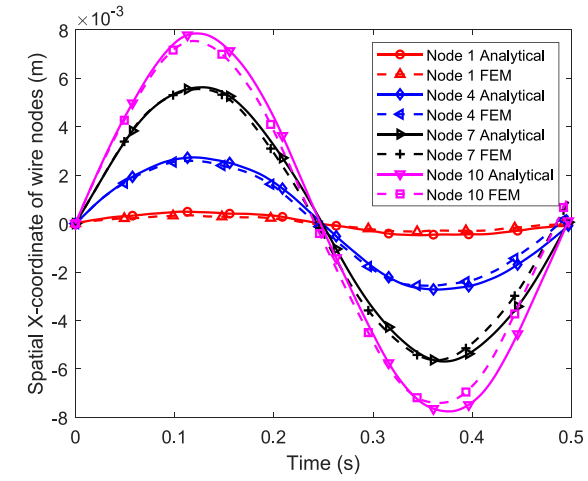

(a)

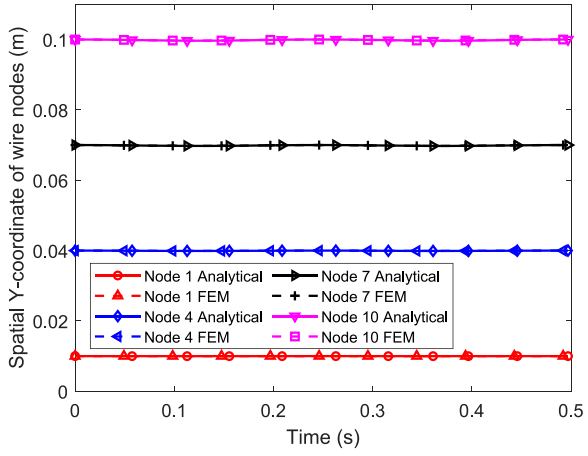

(b)

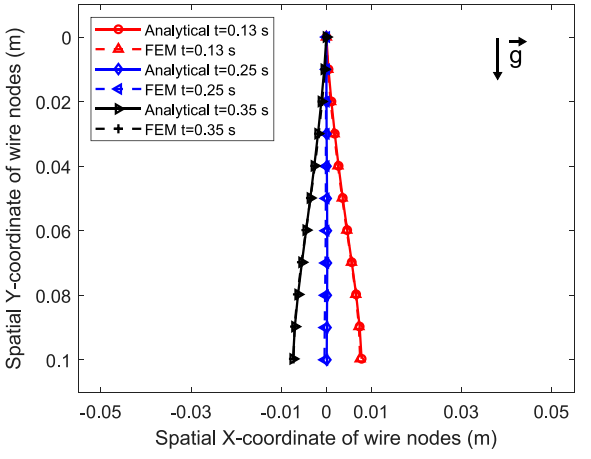

(c)

Fig. 5. Comparison between analytical and FE predictions of a 1D continuous wire discretised with $N = 10$ elements ($\rho = 280$ kg/m^3, $E = 7.2$ GPa, $L = 0.1$, $R = 2.76$ μm) and initial conditions $\theta_{oi} = 0$, $\dot{\theta}_{oi} = 1$ rad/s for all elements, subjected to gravity ($g = 9.81$ m/s^2) and with node 0 pinned. (a) Spatial X-coordinate of nodes 1,4,7 and 10 versus time during an oscillation. (b) Spatial Y-coordinate of nodes 1,4,7 and 10 versus time during an oscillation. (c) Spatial Y-coordinate versus spatial X-coordinate of nodes 1,4,7 and 10 at $t = 0.13$ s, $t = 0.25$ s and $t = 0.35$ s.

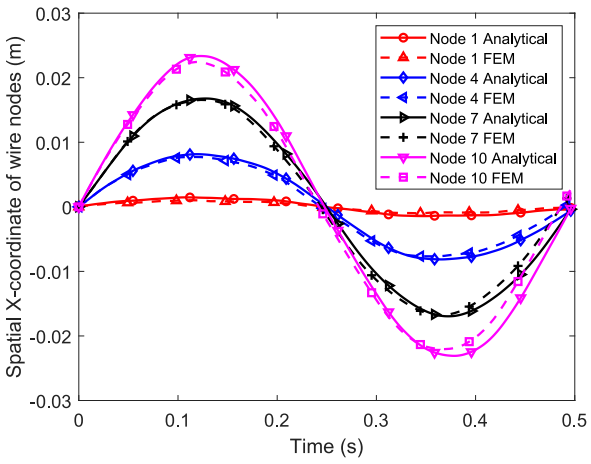

(a)

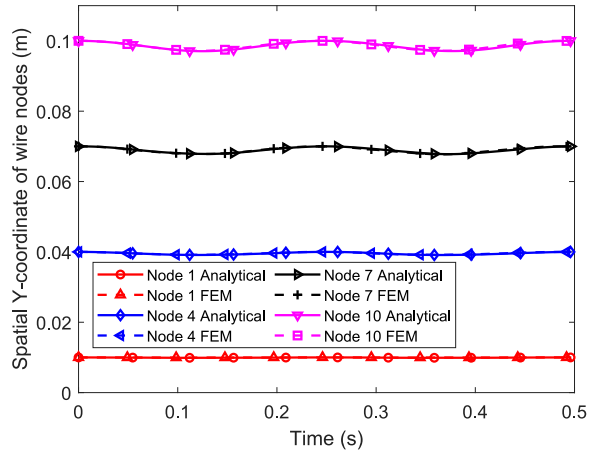

(b)

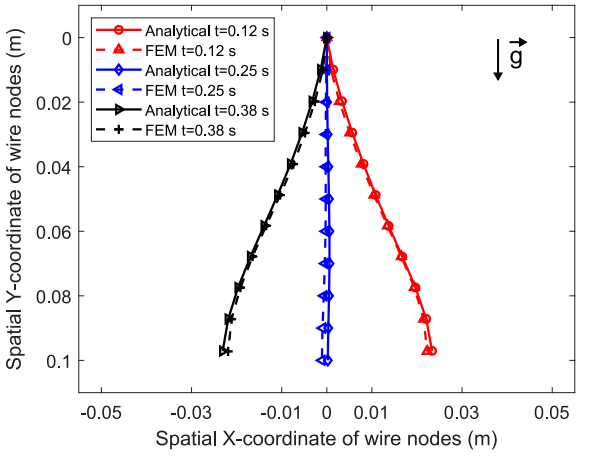

(c)

Fig. 6. Comparison between analytical and FE predictions of a 1D continuous wire discretised with $N = 10$ elements ($\rho = 280$ kg/m^3, $E = 7.2$ GPa, $L = 0.1$, $R = 2.76$ μm) and initial conditions $\theta_{oi} = 0$, $\dot{\theta}_{oi} = 3$ rad/s for all elements, subjected to gravity ($g = 9.81$ m/s^2) and with node 0 pinned. (a) Spatial X-coordinate of nodes 1,4,7 and 10 versus time during an oscillation. (b) Spatial Y-coordinate of nodes 1,4,7 and 10 versus time during an oscillation. (c) Spatial Y-coordinate versus spatial X-coordinate of nodes 1,4,7 and 10 at $t = 0.12$ s, $t = 0.25$ s and $t = 0.38$ s.

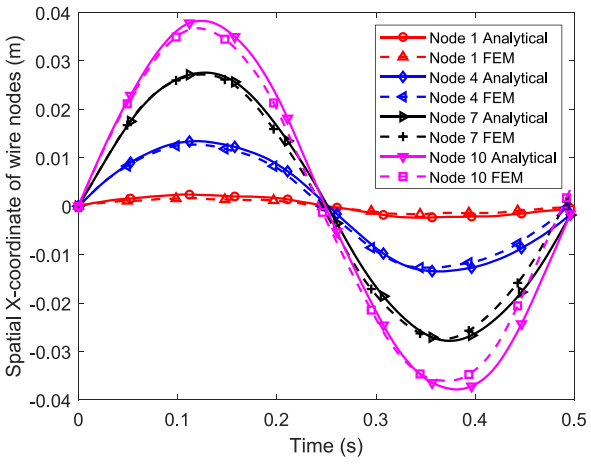

(a)

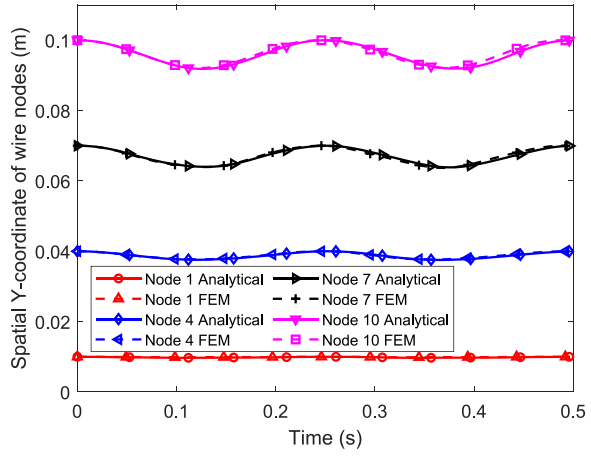

(b)

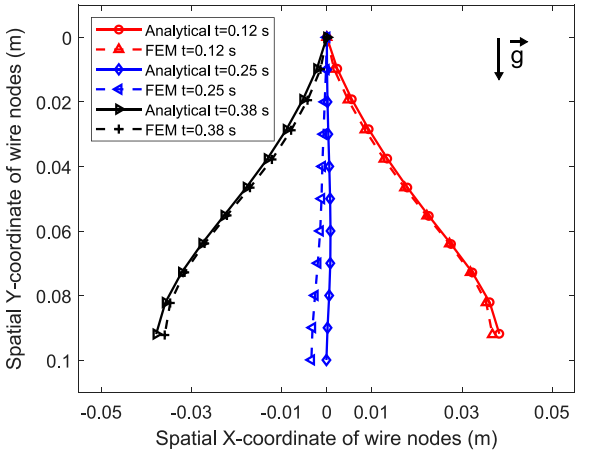

(c)

Fig. 7. Comparison between analytical and FE predictions of a 1D continuous wire discretised with $N = 10$ elements ($\rho = 280$ kg/m^3, $E = 7.2$ GPa, $L = 0.1$, $R = 2.76$ μm) and initial conditions $\theta_{oi} = 0$, $\dot{\theta}_{oi} = 5$ rad/s for all elements, subjected to gravity ($g = 9.81$ m/s^2) and with node 0 pinned. (a) Spatial X-coordinate of nodes 1,4,7 and 10 versus time during an oscillation. (b) Spatial Y-coordinate of nodes 1,4,7 and 10 versus time during an oscillation. (c) Spatial Y-coordinate versus spatial X-coordinate of nodes 1,4,7 and 10 at $t = 0.12$ s, $t = 0.25$ s and $t = 0.38$ s.

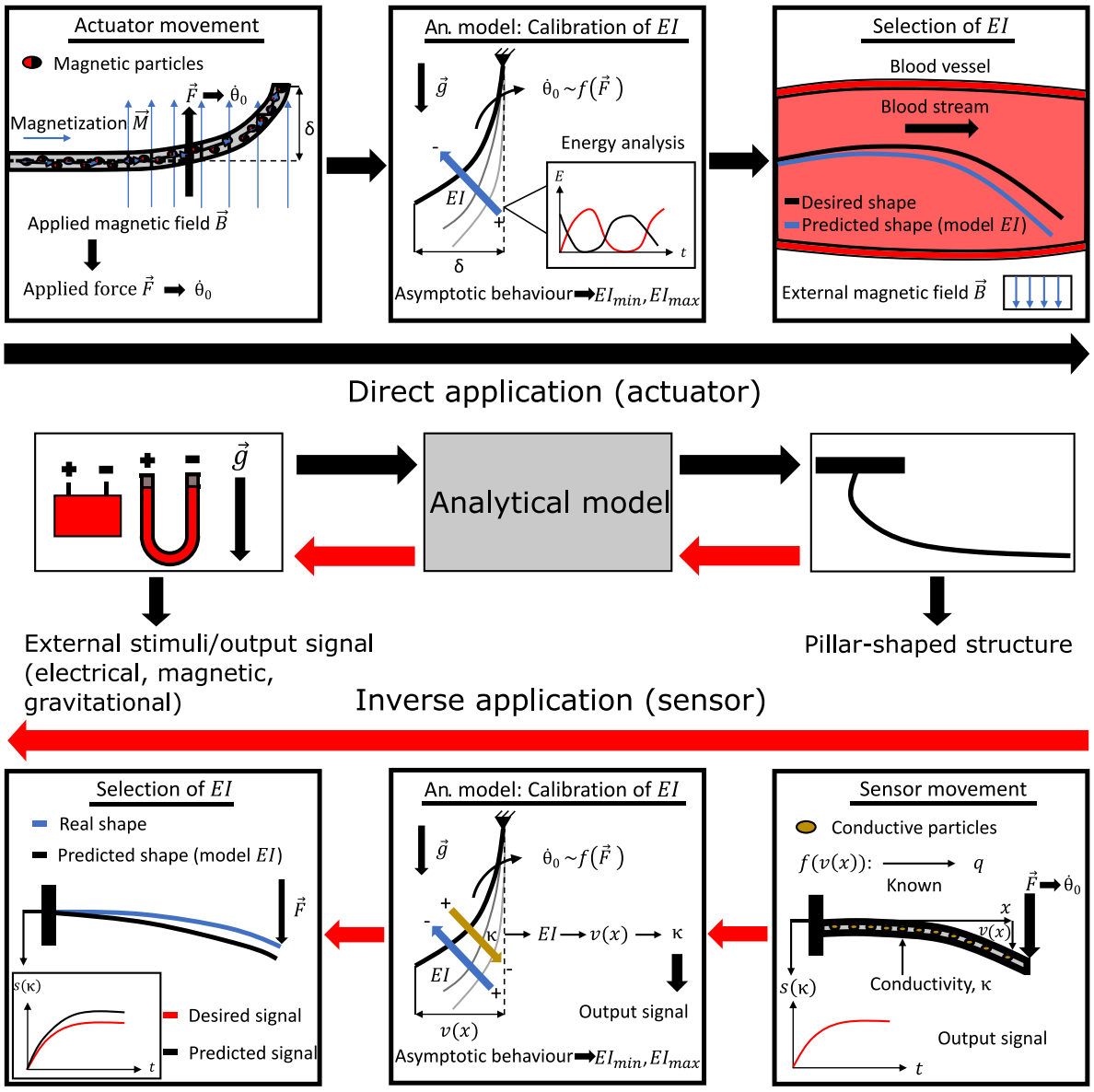

Fig. 8. Concept figure of direct and inverse schemes of application of the analytical model to the calibration of the required bending stiffness, EI, according to the requirements of each application: in the direct application, EI is calibrated to cause a desired movement of a magnetised pillar-shaped actuator when subjected to a magnetic field; in the inverse application, EI is calibrated to provide a required output signal as the conductivity changes because of the movement of the wire.

Overall the predictions observed in Figs. 5–7 positively assess the predictive capability of the analytical model to describe the dynamics of a potentially pillar-shaped bioinspired sensor subjected to an external stimulus brought in by the angular velocity, and reveals that results are not sensitive to the amplitude of the oscillation.

4. Results and discussion: Inverse engineering applications through energy analysis

The model presented is intended to be used for the design of multifunctional pillar-shaped bioinspired sensors, if the motion is turned into a signal, or actuators, if the mechanical response is controlled by an imposed stimulus. Therefore, as Fig. 8 shows, the inverse or direct relationship of a sensor or actuator with an external stimulus (i.e. electric or magnetic signals or a gravitational field) defines the direction of the application. On the one hand, if the mechanical motion of the filament is transformed into a detectable electric signal, the filament will have a sensor-like behaviour within an inverse application. For instance, flexible conductive wires made of conductive particles can be printed on a beam made of soft materials (Fig. 9(a)). The wires can increase or decrease the electric resistance as tension or compression states are induced in the bending process. That is why the conductive filament itself can serve to detect flows due to the bending induced as Fig. 8 shows. The vertical displacement of the filament changes its conductivity and hence, the signal transmitted that must be interpreted to find out the physical phenomenon taking place. Hence, the model proposed can help calibrating the required bending rigidity of the conductive wire, EI, to reach a certain conductivity, κ, to send a signal, $s(\kappa)$, as long as the relationship between shape or deformation and conductivity is known and the actuating force, $\vec{F}$, can be replaced by an initial angular velocity, $\dot{\theta}_0$, causing a response of the same order of magnitude (Fig. 8). Note that the relationship between the external stimulus and the initial conditions/loading may not be direct and has to be studied for each particular problem requiring minor or major changes in the formulation depending on the complexity of the

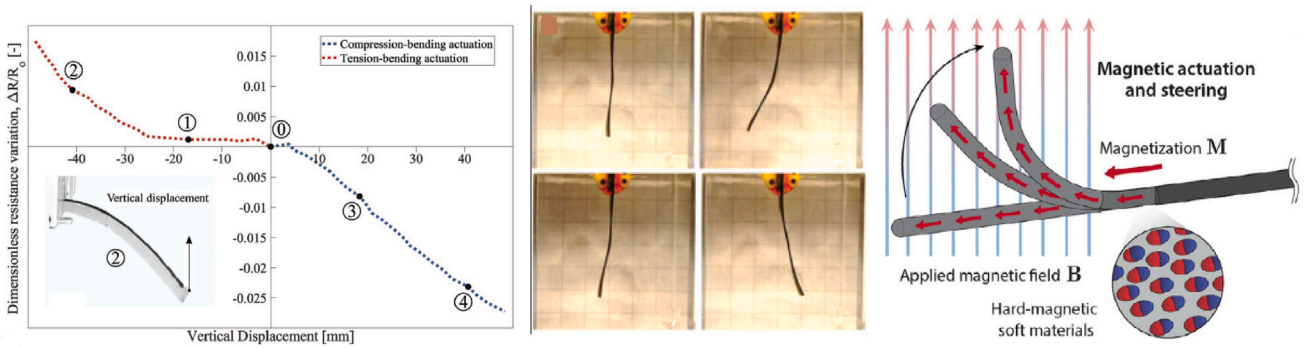

(a) Conductive filament (wire) printed over elastomeric beam in digital ink writing [9]

(b) Ionic polymer-metal composites excited with an electric field [6]

(c) Filament soft polymer matrix subjected to a uniform magnetization [8]

Fig. 9. Examples of bioinspired smart sensors or actuators that either turn a mechanical input into a signal or an external stimulus into a movement.

case. Filament structures based on spider fine hairs constitute another example of sensors serving as wind detectors (Wu et al., 2019).

On the other hand, if the stimulus produces the mechanical response, the structure will have an actuator role for a direct application. For instance, the ionic polymer-metal composites that require low voltage to provide large displacements can swing in opposite directions just inverting the polarity of the electric signal as shown in Fig. 9(b). Another application emerges from the manufacturing of magnetic field-controllable elastomeric fibres with applicability in the endovascular treatment of cardiovascular diseases (Wang et al., 2021): such fibres are enhanced by adding hard-magnetic particles reactive to a constant magnetic field constituting a hard-magnetic elastica (Wang et al., 2020). A scheme of this soft material is shown in Fig. 9(c). The actuation consists of a beam distal portion that can be properly bent in the inside of blood vessels branches or injured tissues. The active bending moment, supposed proportional to the curvature, is calculated as the summation of the magnetic torques in the filament length. The constant of proportionality is the product of Young's modulus multiplied by the static inertia. For that reason, depending on the rigidity needed for a specific application so that the actuator achieves the desired behaviour, the determination of EI, at least qualitatively, becomes crucial. In this sense, the analytical model presented can help calibrating the appropriated EI for an application with the aid of an energy analysis with gravity to find out the asymptotic behaviour of the pillar-shaped structure as long as the imposed force, $\vec{F}$, can be qualitatively related to an initial angular velocity, $\dot{\theta}_0$, provoking a response of the same order of magnitude.

For that purpose, the appraisal of the distribution of energies can serve as a clarifying analysis to understand the physics involved in the problem of a 1D continuous wire subjected to gravity as a way to calibrate the rigidity needed. In this way, the value of EI and its relationship with the wire motion is conceived as an inverse engineering problem.

Being $\theta_j(\bar{t})$ and $\dot{\theta}_j(\bar{t})$ vectors available after solving the system given by Eqs. (18), it is possible to determine the kinetic, potential gravitational and internal strain energies through the expressions deduced above. Moreover, after turning the formulation into non-dimensional (Eq. (15)), a consideration related to the role played by $\bar{g}$ can be pointed out. By definition (see Eqs. (13)), this parameter compares the relative effect of gravity with respect to normal acceleration in the wire extreme, which is established as proportional to the bending stiffness. In this sense, lower values of $\bar{g}$ ($g \ll \omega^2 L \sim EI$) suggest higher centripetal acceleration implying higher internal strain energies due to the higher stiffness of the wire. In contrast, higher values of $\bar{g}$ ($g \gg \omega^2 L$) involves the wire approaches the motion of a simple pendulum, corresponding to humble internal strain energy rates compared to kinetic or gravitational potential energies. Recall that the total motion energy has to be conserved, as gravity is a conservative force and the wire deformation is reversible. In this section, several cases are analysed for different values of $\bar{g}$ using the analytical model proposed. Fig. 10 shows the non-dimensional energy contributions over non-dimensional time for a wire with initial conditions of $\theta_{oi} = 0$ and $\dot{\theta}_{oi} = 14$ for all elements for $\bar{g} = 200$ (Fig. 10(a)), $\bar{g} = 1200$ (Fig. 10(c)) and $\bar{g} = 2000$ (Fig. 10(e)) along with the non-dimensional spatial Y-coordinate versus the non-dimensional spatial X-coordinate of wire nodes (Figs. 10(b), 10(d), 10(f)) for representative instants of time.

In Fig. 10, the distribution of the kinetic energy, $\bar{T}$ (Eq. (20)), gravitational potential energy[16], $\bar{V}_g$ (Eq. (22)), and internal strain energy, $\bar{V}_e$ (Eq. (25)), versus non-dimensional time, $\bar{t}$, is represented for the referred values of $\bar{g}$. The potential, $\bar{V}_p$, and total energy, $\bar{E}$, are likewise taken in consideration[17]. In each case, the integration time is chosen so that the wire approximately swings one complete oscillation. As mentioned above, several positions of the wire are shown in characteristic instants of time for each value of $\bar{g}$. Such positions represented in Figs. 10(b), 10(d) and 10(f) are highlighted with Greek characters and star markers in Figs. 10(a), 10(c) and 10(e), respectively.

For all cases, the first instant, α, indicates the maximum of the kinetic energy at the beginning of motion and provided by the initial condition. β and γ instants are defined in the relative maximum of potential and gravitational energies, respectively, being the reference for the gravitational energy the initial extended position of the wire. δ instant coincides with a relative maximum of the internal strain energy which is alike situated in the extreme. An intermediate situation occur at ε instant, in which kinetic and potential energies acquire the same value. Lastly, ξ instant represents a local minimum of potential energy, which happens to be in the initial position.

In the light of the results, a full complete oscillation needs for smaller periods of time as $\bar{g}$ increases. This result admits a logical interpretation since the effect of gravity, as the cause of motion, becomes more important. Fig. 10 shows that energies distribution behaves as a typical energetic interchange of a conservative oscillatory problem. As the kinetic energy grows maximum, the potential energy becomes null minimising the internal strain and gravitational energies. As shown in Figs. 10(b), 10(d) and 10(f), the wire behaviour approaches the one of a simple pendulum as $\bar{g}$ increases, for the same initial velocity in all elements and cases. This fact produces that the wire presents smaller oscillations. This is in agreement with the explanation previously provided implying that smaller values of $\bar{g}$ lead to higher internal strain energy rates. It is also worthy to observe that ε instant does not occur in the intermediate exact position between β and ξ, being closer to

[16] With respect to $\bar{V}_{og}$ (see Eq. (23)). This means that the referred $\bar{V}_g$ in Fig. 10 must be understood as $\bar{V}_g - \bar{V}_{og}$.

[17] As $\bar{V}_g - \bar{V}_{og} + \bar{V}_e$ and $\bar{T} + \bar{V}_p$, respectively.

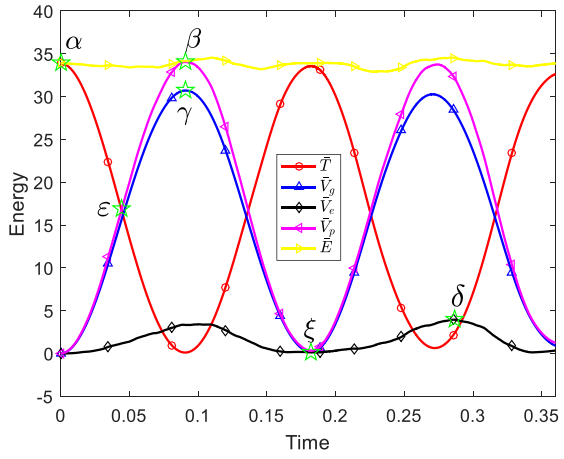

(a) Energies distribution. Case $\bar{g} = 200$

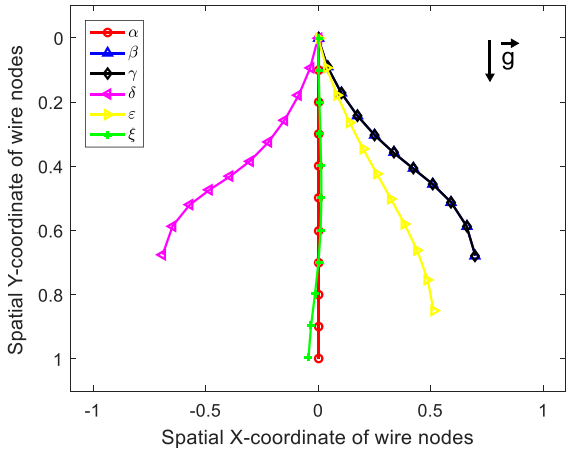

(b) Wire positions. Case $\bar{g} = 200$

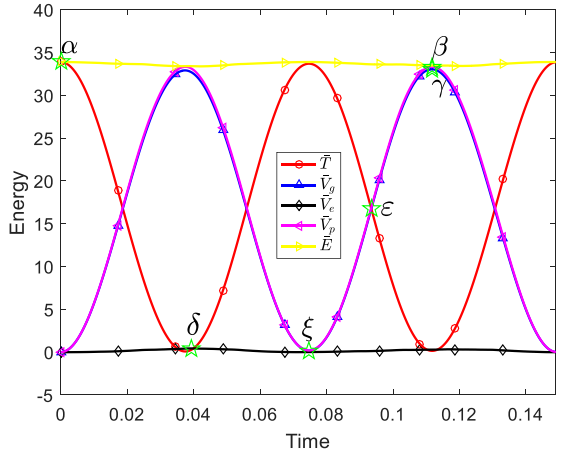

(c) Energies distribution. Case $\bar{g} = 1200$

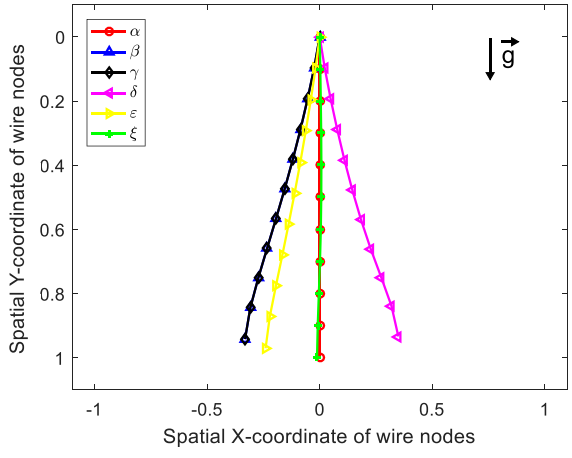

(d) Wire positions. Case $\bar{g} = 1200$

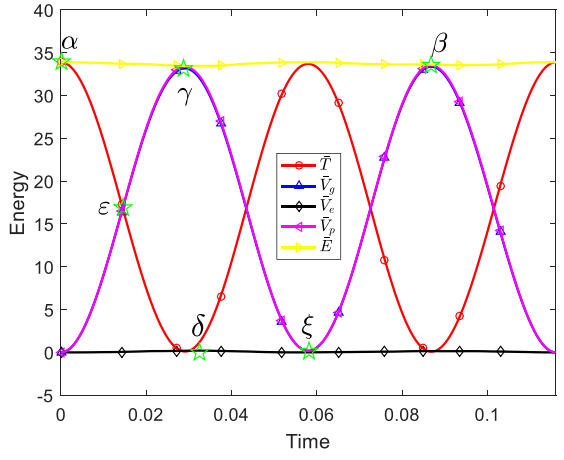

(e) Energies distribution. Case $\bar{g} = 2000$

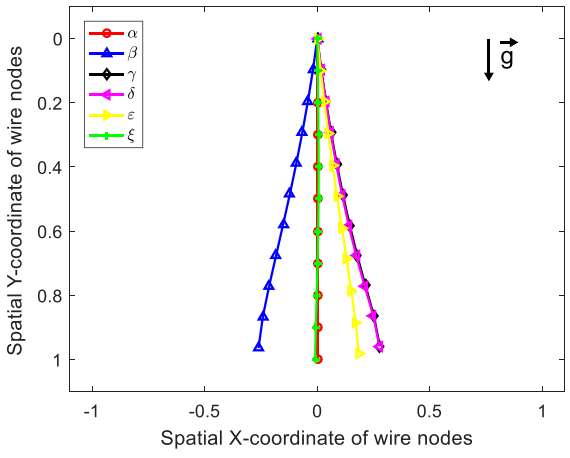

(f) Wire positions. Case $\bar{g} = 2000$

Fig. 10. Non-dimensional representation of the wire motion discretised with $N = 10$ elements and initial conditions $\theta_{ai} = 0$, $\dot{\theta}_{ai} = 14$ for all elements, subjected to gravity and with node 0 pinned.

the β (or γ) in all cases as Figs. 10(b), 10(d) and 10(f) show. This is a consequence of the non-linearity of Eqs. (18).

Finally, it is interesting to give insights into the sources of numerical inaccuracies related to the discretisation methods used. In principle, the main cause of error lies on the finite difference formulas to approximate the derivatives needed to calculate $\bar{V}_e$. For this reason, in all cases where internal strain energy becomes important, a less accurate calculation is expected. An indicator of that is the mild oscillation of $\bar{E}$

values around the initial total energy, which should be theoretically conserved. As it can be observed in Figs. 10(a), 10(c) and 10(e), the oscillations from initial energy tend to be null as $\bar{g}$ increases in behalf of the reduction of the internal strain energy for those cases. However, the relative error of the total energy with respect to the initial energy is less than 3% in all cases; therefore, the referred inaccuracies are considered to be no relevant: on the one hand, the total energy oscillates around a constant value which is indeed preserved over time, corresponding to the total energy of the system. On the other hand, low values of $\bar{g}$ correspond to sufficiently degenerated cases, so that the range of applicability with negligible errors is still wide. Furthermore, the previous indicates that numerical inaccuracies are not cumulative. Another indicator of the referred errors is the deviation at the wire free end with respect to the initial position at ξ instant, which should be coincident with α instant in Fig. 10(b) given the conservative nature of the problem. As already stated, low values of $\bar{g}$ implies relevant centripetal acceleration compared to gravity which is maximised precisely at the free end. As said, this normal acceleration is proportional to EI producing higher values in internal strain energy and provoking larger numerical errors. In correspondence, such deviation results to be oscillatory around the initial position which is well captured in the cases corresponding to higher values of $\bar{g}$.

The analysis carried out with the aid of gravity allows to qualitatively locate EI between the asymptotic behaviours of a more rigid or flexible wire under an external action (Fig. 8). The model determines the mechanical motion of the wire structure in agreement with EI. In the cardiovascular disease example (Wang et al., 2021), depending on the flexibility required according to the order of magnitudes of the problem, this methodology elucidates the qualitative calibration of EI. Overall, the analysis performed with the energies of the pillar-shaped structure constitutes an example of the potential quantitative analyses this model can provide to infer qualitative conclusions that cooperate in the conceptualisation and layout of bioinspired sensors.

5. Conclusions

Smart materials relating their mechanical response to an applied stimulus or a transmitted signal has become a high-impact solution to multiple applications: from heart diseases to the detection of wind presence, human breath or shape-morphing actuation. In this paper, pillar-shaped structures bioinspired in examples from nature are studied. The methodology proposed allows for a concise comprehension of the mechanical motion of the wire subjected to constant fields. The model deals with the intermediate phase to connect the inputs with the outputs. Therefore, two different senses of application can serve to sort out the use of a pillar-shaped structure; if the system serves as an actuator (direct) the motion of the filament is stimulated by exposing the structure to an electrical/magnetic or simply the gravitational field. Otherwise, the wire is conceived as a sensor (inverse) that can send different signals triggered by the wire motion when exposed to external stimuli.

In this work, a new model to properly describe a 1D pillar-shaped inextensible structure under initial conditions and gravity was exposed. The inextensibility hypothesis is a limitation to the model that can only be used in those cases in which such assumption is reasonable. Among others, some examples taken from recent literature were exposed in Fig. 9. A discretisation was performed to approximate the terms of the integro-differential governing equation such as the bending internal effort derivatives through midpoint rules and centred FDM schemes. These terms were compacted in several matrices and vectors originally defined. As a result, an IVP was formulated helping the physics involved to be identified. The initial conditions are understood in the intermediate phase as an impulsive stimulus accounting for the external action on the wire. The non-dimensional formulation proposed revealed the only non-dimensional group which the problem depends on. Such parameter compares the relative effect of gravity with the wire normal acceleration, being proportional to the wire bending rigidity. Additionally, expressions to account for the kinetic, gravitational potential and internal strain energies were implemented using the same discretisation matrices and FDM approximation formulas, allowing for the physical interpretation of the results. Moreover, a validation comparing the results obtained with a separate FE approach confirmed the capability of the proposed model to describe the 2D wire motion in spite of the oscillation amplitude under gravity and initial conditions coming from external actions.

The physical meaning of the non-dimensional group governing the problem allows to establish a direct correspondence between the bending rigidity and the shape of the wire, providing a qualitatively guide to anticipate the wire mechanical performance between two asymptotic cases. The model is able to explain the energy interchange corresponding to an oscillating motion. As the non-dimensional parameter increases when keeping the IVP initial conditions unchanged, the wire motion goes from presenting large deformations and high internal energy strain rates to behave similar to a simple pendulum, oscillating close to the initial position, and implying lower internal energy strain rates and smaller deformations. This behaviour can be tuned through the non-dimensional parameter, which implies the bending rigidity, to achieve a specific motion needed when subjected to an external action to help designing actuators or sensors within direct or inverse applications.

The higher computational cost and general inability to work within modular automated models of FE approaches make analytical models a desirable tool to tackle the design of bioinspired smart sensors. The extracted conclusions obtained from simple models to describe the motion of a 1D wire subjected to a constant field can help solving inverse-engineering problems, and serve as an inspiration in the generation of more complex and concrete solutions. Finally, the versatility of the model hands over the possibility of introducing different motion sources by changing the gravity term in the equations, and, in future developments, considering different charge densities along the pillar-shaped structure. As a consequence, the actual proposal can prompt more concrete applications, devoting future works to generalise and adapt the model for high-impact applications. In this sense, the potential applicability to non-constant fields may require the spatial discretisations of the constitutive equations in such problems and the revision of the formulation given above.

CRediT authorship contribution statement

A. Solis: Writing – review & editing, Writing – original draft, Validation, Supervision, Software, Methodology, Investigation, Formal analysis, Conceptualization. **L. Alonso:** Writing – review & editing, Writing – original draft, Validation, Supervision, Software, Methodology, Investigation, Formal analysis, Conceptualization.

Declaration of competing interest

The authors declare that they have no known competing financial interests or personal relationships that could have appeared to influence the work reported in this paper.

Data availability

Data will be made available on request.

Acknowledgements

The authors would like to acknowledge the reviewing and editing support received from Vanesa Muñoz-Perales.

References

Bastola, A.K., Hossain, M., 2021. The shape – morphing performance of magnetoactive soft materials. Mater. Des. 211, 110172. http://dx.doi.org/10.1016/j.matdes.2021.110172, URL: https://www.sciencedirect.com/science/article/pii/S0264127521007279.

Cheng, Y., Ma, Y., Li, L., Zhu, M., Yue, Y., Liu, W., Wang, L., Jia, S., Li, C., Qi, T., Wang, J., Gao, Y., 2020. Bioinspired microspines for a high-performance spray Ti3C2Tx mxene-based piezoresistive sensor. ACS Nano 14 (2), 2145–2155. http://dx.doi.org/10.1021/acsnano.9b08952, arXiv:https://doi.org/10.1021/acsnano.9b08952, PMID: 32040310.

Entov, V.M., Yarin, A.L., 1984. The dynamics of thin liquid jets in air. J. Fluid Mech. 140, 91–111. http://dx.doi.org/10.1017/S0022112084000525.

Garcia-Gonzalez, D., Ter-Yesayants, T., Moreno-Mateos, M.A., Lopez-Donaire, M.L., 2023. Hard-magnetic phenomena enable autonomous self-healing elastomers. Composites B 248, 110357. http://dx.doi.org/10.1016/j.compositesb.2022.110357, URL: https://www.sciencedirect.com/science/article/pii/S1359836822007302.

Ilami, M., Bagheri, H., Ahmed, R., Skowronek, E.O., Marvi, H., 2021. Materials, actuators, and sensors for soft bioinspired robots. Adv. Mater. 33 (19), 2003139. http://dx.doi.org/10.1002/adma.202003139, URL: https://onlinelibrary.wiley.com/doi/abs/10.1002/adma.202003139.

Kiang, J.D., Wen, J.H., Del Álamo, J.C., Engler, A.J., 2013. Dynamic and reversible surface topography influences cell morphology.

Kim, Y., Yuk, H., Zhao, R., Chester, S.A., Zhao, X., 2018. Printing ferromagnetic domains for untethered fast-transforming soft materials. Nature 558, http://dx.doi.org/10.1038/s41586-018-0185-0.

Lopez-Donaire, M.L., de Aranda-Izuzquiza, G., Garzon-Hernandez, S., Crespo-Miguel, J., Fernandez-de la Torre, M., Velasco, D., Garcia-Gonzalez, D., 2023. Computationally guided DIW technology to enable robust printing of inks with evolving rheological properties. Adv. Mater. Technol. 8 (3), 2201707. http://dx.doi.org/10.1002/admt.202201707, URL: https://onlinelibrary.wiley.com/doi/abs/10.1002/admt.202201707.

Lu, H., Zhang, M., Yang, Y., Huang, Q., Fukuda, T., Wang, Z., Shen, Y., 2018. A bioinspired multilegged soft millirobot that functions in both dry and wet conditions. Nature Commun. 9, http://dx.doi.org/10.1038/s41467-018-06491-9.

Mahadevan, L., Keller, J.B., 1996. Coiling of flexible ropes. Proc. R. Soc. Lond. Ser. A Math. Phys. Eng. Sci. 452 (1950), 1679–1694. http://dx.doi.org/10.1098/rspa.1996.0089.

Moreno-Mateos, M.A., Hossain, M., Steinmann, P., Garcia-Gonzalez, D., 2023. Hard magnetics in ultra-soft magnetorheological elastomers enhance fracture toughness and delay crack propagation. J. Mech. Phys. Solids 173, 105232. http://dx.doi.org/10.1016/j.jmps.2023.105232, URL: https://www.sciencedirect.com/science/article/pii/S0022509623000364.

Moreno-Mateos, M.A., Lopez-Donaire, M.L., Hossain, M., Garcia-Gonzalez, D., 2022. Effects of soft and hard magnetic particles on the mechanical performance of ultra-soft magnetorheological elastomers. Smart Mater. Struct. 31 (6), 065018. http://dx.doi.org/10.1088/1361-665X/ac6bd3.

Mukherjee, D., Danas, K., 2022. A unified dual modeling framework for soft and hard magnetorheological elastomers. Int. J. Solids Struct. 257, 111513. http://dx.doi.org/10.1016/j.ijsolstr.2022.111513, URL: https://www.sciencedirect.com/science/article/pii/S0020768322000725, Special Issue in the honour Dr Stelios Kyriakides.

Park, J., Lee, Y., Hong, J., Lee, Y., Ha, M., Jung, Y., Lim, H., Kim, S.Y., Ko, H., 2014. Tactile-direction-sensitive and stretchable electronic skins based on human-skin-inspired interlocked microstructures. ACS Nano 8 (12), 12020–12029. http://dx.doi.org/10.1021/nn505953t, PMID: 25389631.

Perez-Garcia, C., Aranda-Ruiz, J., Lopez-Donaire, M.L., Zaera, R., Garcia-Gonzalez, D., 2024. Magneto-responsive bistable structures with rate-dependent actuation modes. Adv. Funct. Mater. 2313865. http://dx.doi.org/10.1002/adfm.202313865.

Rambausek, M., Mukherjee, D., Danas, K., 2022. A computational framework for magnetically hard and soft viscoelastic magnetorheological elastomers. Comput. Methods Appl. Mech. Engrg. 391, 114500. http://dx.doi.org/10.1016/j.cma.2021.114500, URL: https://www.sciencedirect.com/science/article/pii/S0045782521007064.

Ribe, N.M., 2004. Coiling of viscous jets. Proc. R. Soc. Lond. Ser. A Math. Phys. Eng. Sci. 460 (2051), 3223–3239. http://dx.doi.org/10.1098/rspa.2004.1353.

Shen, Q., Trabia, S., Stalbaum, T., Palmre, V., Kim, K., Oh, I.-K., 2016. A multiple-shape memory polymer-metal composite actuator capable of programmable control, creating complex 3D motion of bending, twisting, and oscillation. Sci. Rep. 6, http://dx.doi.org/10.1038/srep24462.

Wang, L., Kim, Y., Guo, C.F., Zhao, X., 2020. Hard-magnetic elastica. J. Mech. Phys. Solids 142, http://dx.doi.org/10.1016/j.jmps.2020.104045.

Wang, W.-Y., Lin, B.-Y., Liao, Y.-P., Yang, Y.-J., 2022b. Photothermal thin films with highly efficient NIR conversion for miniaturized liquid-crystal elastomer actuators. Polymers 14 (15), http://dx.doi.org/10.3390/polym14152997, URL: https://www.mdpi.com/2073-4360/14/15/2997.

Wang, C., Tang, H., Zhang, X., 2022a. Fluid-structure interaction of bio-inspired flexible slender structures: a review of selected topics. Bioinspiration Biomim. 17 (4), 041002. http://dx.doi.org/10.1088/1748-3190/ac68ba.

Wang, L., Zheng, D., Harker, P., Patel, A.B., Guo, C.F., Zhao, X., 2021. Evolutionary design of magnetic soft continuum robots. Proc. Natl. Acad. Sci. USA 118 (21), e2021922118. http://dx.doi.org/10.1073/pnas.2021922118, URL: https://europepmc.org/articles/PMC8166154.

Wu, Z., Ai, J., Ma, Z., Zhang, X., Du, Z., Liu, Z., Chen, D., Su, B., 2019. Flexible out-of-plane wind sensors with a self-powered feature inspired by fine hairs of the spider. ACS Appl. Mater. Interfaces 11 (47), 44865–44873. http://dx.doi.org/10.1021/acsami.9b15382, PMID: 31686494.

Wu, Y., Dong, X., kang Kim, J., Wang, C., Sitti, M., 2022. Wireless soft millirobots for climbing three-dimensional surfaces in confined spaces. Sci. Adv. 8 (21), eabn3431. http://dx.doi.org/10.1126/sciadv.abn3431, arXiv:https://www.science.org/doi/pdf/10.1126/sciadv.abn3431, URL: https://www.science.org/doi/abs/10.1126/sciadv.abn3431.

Xiong, Y., Shen, Y., Tian, L., Hu, Y., Zhu, P., Sun, R., Wong, C.-P., 2020. A flexible, ultra-highly sensitive and stable capacitive pressure sensor with convex microarrays for motion and health monitoring. Nano Energy 70, 104436. http://dx.doi.org/10.1016/j.nanoen.2019.104436, URL: https://www.sciencedirect.com/science/article/pii/S221128551931153X.

Zhang, J., Hao, L., Yang, F., Jiao, W., Liu, W., Li, Y., Wang, R., He, X., 2016. Biomimic hairy skin tactile sensor based on ferromagnetic microwires. ACS Appl. Mater. Interfaces 8 (49), 33848–33855. http://dx.doi.org/10.1021/acsami.6b14236, PMID: 27960407.

Zhang, C., Ye, W.B., Zhou, K., Chen, H.-Y., Yang, J.-Q., Ding, G., Chen, X., Zhou, Y., Zhou, L., Li, F., Han, S.-T., 2019. Bioinspired artificial sensory nerve based on nafion memristor. Adv. Funct. Mater. 29 (20), 1808783. http://dx.doi.org/10.1002/adfm.201808783, URL: https://onlinelibrary.wiley.com/doi/abs/10.1002/adfm.201808783.

Zhao, S., Ahn, J.-H., 2022. Rational design of high-performance wearable tactile sensors utilizing bioinspired structures/functions, natural biopolymers, and biomimetic strategies. Mater. Sci. Eng. R 148, 100672. http://dx.doi.org/10.1016/j.mser.2022.100672.

Zhao, X., Chen, F., Li, Y., Lu, H., Zhang, N., Ma, M., 2018. Bioinspired ultra-stretchable and anti-freezing conductive hydrogel fibers with ordered and reversible polymer chain alignment. Nature Commun. 9.

Zhu, Z., Ng, D.W.H., Park, H.S., McAlpine, M.C., 2021. 3D-printed multifunctional materials enabled by artificial-intelligence-assisted fabrication technologies. Nat. Rev. Mater. 6 (1), http://dx.doi.org/10.1038/s41578-020-00235-2.